Functional role of T-cell receptor nanoclusters in signal initiation and antigen discrimination

Sophie V. Pageon[a,b,1], Thibault Tabarin[a,b,1], Yui Yamamoto[a,b,1], Yuanqing Ma[a,b], Philip R. Nicovich[a,b], John S. Bridgeman[c,d], André Cohnen[e], Carola Benzing[a,b], Yijun Gao[a,b], Michael D. Crowther[c], Katie Tungatt[c], Garry Dolton[c], Andrew K. Sewell[c], David A. Price[c,f], Oreste Acuto[e], Robert G. Parton[g,h,i], J. Justin Gooding[i,j], Jérémie Rossy[a,b], Jamie Rossjohn[c,k,l], and Katharina Gaus[a,b,2]

[a]European Molecular Biology Laboratory (EMBL) Australia Node in Single Molecule Science, School of Medical Sciences, University of New South Wales, Sydney, NSW 2052, Australia; [b]Australian Research Council Centre of Excellence in Advanced Molecular Imaging, University of New South Wales, Sydney, NSW 2052, Australia; [c]Institute of Infection and Immunity, Cardiff University School of Medicine, Cardiff CF14 4XN, United Kingdom; [d]Cellular Therapeutics Ltd., Manchester M13 9XX, United Kingdom; [e]T Cell Signalling Laboratory, Sir William Dunn School of Pathology, University of Oxford, Oxford OX1 3RE, United Kingdom; [f]Human Immunology Section, Vaccine Research Center, National Institute of Allergy and Infectious Diseases, National Institutes of Health, Bethesda, MD 20892; [g]Institute for Molecular Bioscience, University of Queensland, St. Lucia, QLD 4072, Australia; [h]Australia Centre for Microscopy and Microanalysis, University of Queensland, St. Lucia, QLD 4072, Australia; [i]Australian Research Council Centre of Excellence in Convergent Bio-Nano Science and Technology, University of Queensland, St. Lucia, QLD 4072, Australia; [j]School of Chemistry and Australian Centre of NanoMedicine, University of New South Wales, Sydney, NSW 2052, Australia; [k]Infection and Immunity Program, Department of Biochemistry and Molecular Biology, Biomedicine Discovery Institute, Monash University, Clayton, VIC 3800, Australia; and [l]Australian Research Council Centre of Excellence in Advanced Molecular Imaging, Monash University, Clayton, VIC 3800, Australia

Antigen recognition by the T-cell receptor (TCR) is a hallmark of the adaptive immune system. When the TCR engages a peptide bound to the restricting major histocompatibility complex molecule (pMHC), it transmits a signal via the associated CD3 complex. How the extracellular antigen recognition event leads to intracellular phosphorylation remains unclear. Here, we used single-molecule localization microscopy to quantify the organization of TCR–CD3 complexes into nanoscale clusters and to distinguish between triggered and nontriggered TCR–CD3 complexes. We found that only TCR–CD3 complexes in dense clusters were phosphorylated and associated with downstream signaling proteins, demonstrating that the molecular density within clusters dictates signal initiation. Moreover, both pMHC dose and TCR–pMHC affinity determined the density of TCR–CD3 clusters, which scaled with overall phosphorylation levels. Thus, TCR–CD3 clustering translates antigen recognition by the TCR into signal initiation by the CD3 complex, and the formation of dense signaling-competent clusters is a process of antigen discrimination.

TCR triggering | signal transduction | single-molecule localization microscopy

The activation of T cells orchestrates an adaptive immune response by translating antigen binding to the T-cell receptor (TCR) into appropriate cellular responses (1–4). The αβ TCR engages MHC molecules (or HLA) bound to antigenic peptides (pMHC) on the surface of antigen-presenting cells (5). The interaction of the TCR with pMHC is highly specific because T cells are able to distinguish rare foreign pMHC among abundant self pMHC molecules (6). TCR signaling is also extremely sensitive; even a single pMHC molecule is sufficient to trigger activation (7–9). TCRs are noncovalently coupled to the conserved multisubunit CD3 complex, comprising CD3εγ, CD3εδ, and CD3ζζ dimers (10), whose immunoreceptor tyrosine-based activation motifs (ITAMs) are phosphorylated upon pMHC engagement by the nonreceptor tyrosine kinase Lck (1, 2). ITAM phosphorylation is required for the recruitment and phosphorylation of the ζ-chain-associated protein kinase 70 kDa (Zap70) and the adaptor linker for activation of T cells (Lat) (11) to mediate downstream activation responses (12). Phosphorylation of the TCR–CD3 complex is one of the earliest detectable biochemical events in T-cell signaling and already at this level, important "activation decisions" are being made. For example, when the extent of ITAM phosphorylation was modulated through specific mutations, low levels of TCR–CD3 phosphorylation were sufficient for signaling through the Zap70–SLP-76–Lat pathway and cytokine production, whereas high levels

of TCR–CD3 phosphorylation were required for Vav1-Numb-Notch signaling and T-cell proliferation (12–14). However, how the TCR–CD3 complex encodes both the quality and quantity of pMHC molecules and steers signaling activities toward appropriate cellular outcomes is not fully understood (1–4).

Although many of the molecular players and TCR signaling pathways have been identified and characterized by biochemical and genetic approaches (12, 15), the precise mechanism by which the binding of the TCR to pMHC results in phosphorylation of the TCR–CD3 complex, referred to as TCR triggering, still remains contested (1, 16). There is increasing evidence that the spatial reorganization of the TCR into micrometer- and submicron-sized clusters is involved in regulating T-cell activation (2, 11, 17–19). With the advent of superresolution fluorescence microscopy, we have gained a much more nuanced picture of the spatial organization of TCR signaling proteins (3, 20). In particular, single-molecule localization microscopy [SMLM, including photoactivated localization microscopy (PALM) (21) and direct

Significance

T-cell activation requires the translation of antigen binding to the T-cell receptor (TCR) into intracellular signaling. However, how antigen recognition and signal transduction are mechanistically linked is poorly understood. Here, we used single-molecule localization microscopy to link TCR clustering to signaling. We found that the likelihood of a single receptor to initiate signaling upon ligand binding depended on receptor-to-receptor spacing, with TCRs in dense clusters having the highest signaling efficiency. This means that antigen recognition must first be translated into a spatial reorganization of receptors into dense, signaling-competent clusters before signaling can begin. Thus, the quality of an antigen in terms of signaling is given by its ability to densely cluster receptors.

stochastic optical reconstruction microscopy (dSTORM) (22)] was used to report that at least a proportion of TCRs were organized into small clusters that were 30–300 nm in diameter, termed "nanoclusters" (23, 24). Similarly, Lat (23–25), Lck (26), and Zap70 (24, 27) were also found to reside in nanoclusters that are extensively remodeled during T-cell activation. The link between preexisting and pMHC-induced nanoclustering and signaling activities is not clear at present and is the focus of the present study.

To identify the functional role of TCR nanoclusters, we used two-color SMLM data and integrated a cluster detection method, density-based spatial clustering of applications with noise (DBSCAN) (28) with a customized colocalization analysis (29). This process allowed us to distinguish phosphorylated from nonphosphorylated TCR–CD3 complex clusters in intact T cells and identify the spatial organization at which individual TCR–CD3 complexes had the highest signaling efficiency. We found that not all TCR–CD3 complexes had the same likelihood of being phosphorylated, even with excess doses of high-affinity pMHC molecules. The signaling efficiency of the TCR–CD3 complex was dependent upon the distance to neighboring complexes so that dense nanoclusters had the highest TCR triggering efficiency.

Results

CD3ζ Molecules Exist in Nanoclusters That Increase in Molecular Density upon T-Cell Activation. To directly link antigen recognition to signal initiation, we aimed to establish single-molecule maps that contained both the spatial organization and the signaling (i.e., phosphorylation) status of the TCR–CD3 complex. Because CD3ζ faithfully reports the localization of the TCR–CD3 complex (30), we fused CD3ζ to the photoactivatable fluorescent protein PSCFP2 and expressed the CD3 dimers in conjunction with three different MHC class I (MHC-I) –restricted αβ TCRs: (*i*) the human ILA1 TCR that recognizes the HLA-A2–restricted peptide ILAKFLHWL (ILA) (31); (*ii*) the human 1G4 TCR that recognizes the HLA-A2–restricted peptide SLLMWITQC (32); and (*iii*) the mouse OT-I TCR that recognizes the H-2K^b-restricted peptide SIINFEKL (*OVA*) (33). We used Jurkat cells transduced to express OT-I (Jurkat–OT-I) and ILA1 (Jurkat–ILA1) and CRISPR/Cas9 gene-edited Jurkat cells expressing 1G4 (deficient in endogenous CD3ζ expression; Jurkat–1G4), as well as primary mouse OT-I CD8$^+$ T cells. Cells were imaged by PALM after stimulation on two types of surfaces: (*i*) glass coverslips coated either with poly-L-lysine (PLL, nonactivating) or with anti-CD3ε and anti-CD28 antibodies (αCD3+αCD28, activating) (Fig. 1*A*); and (*ii*) supported lipid bilayers containing either intercellular adhesion molecule 1 (ICAM-1, nonactivating) or ICAM-1 and pMHC-I molecules (activating) (Fig. 1*A*). Whereas immobilized antibodies trigger the TCR and induce early T-cell signaling, including phosphorylation of CD3ζ (pCD3ζ) (Fig. 1*B*), T cells on laterally mobile bilayers form a spatial arrangement, known as the immunological synapse (11, 26, 34), where the TCR–CD3 complex accumulates in the central region (Fig. 1*A*). Phosphorylated CD3ζ (pCD3ζ) was stained with phospho-specific antibodies and imaged by dSTORM (22, 35). Both CD3ζ–PSCFP2 and immunostained pCD3ζ could be localized with <30-nm positional accuracy (*SI Appendix*, Fig. S1 *A* and *B*).

A global distribution analysis based on Ripley's *K*-function (26, 36) (*SI Appendix*, Fig. S1 *C* and *D*) revealed that CD3ζ–PSCFP2 was less randomly distributed in activated T cells compared with resting T cells, independent of antibody versus pMHC-I stimulation (*SI Appendix*, Fig. S2), confirming previous findings (23, 26). To identify nanoscale clusters within an image, we implemented a cluster detection analysis called DBSCAN (28), which links only closely packed points together in a propagative manner (*SI Appendix*, Fig. S3 *A* and *B*). We could thus identify molecules within and outside clusters with diameters of 84 ± 9 nm (αCD3+αCD28) and 102 ± 20 nm (ICAM-1 + OVA) (Fig. 1*A*). Antibody
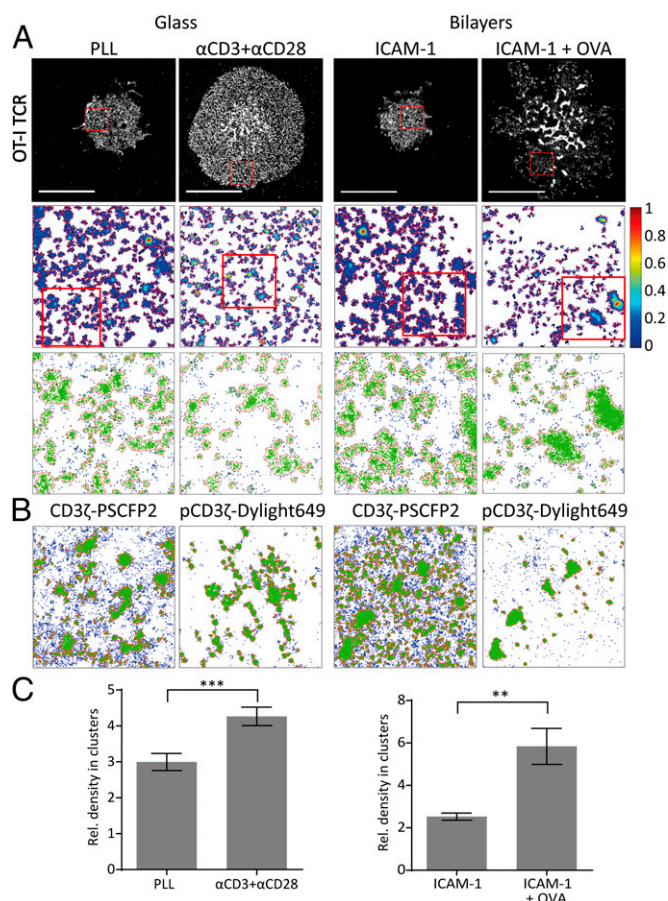

Fig. 1. TCR activation-induced CD3ζ clustering. (*A, Top*) Single-molecule images of CD3ζ–PSCFP2 in Jurkat–OT-I cells on resting (PLL-coated) or antibody-coated (anti-CD3ε and anti-CD28 antibodies, αCD3+αCD28) glass surfaces (*Left*, 10 min) and on supported lipid bilayers (*Right*, 15 min) containing ICAM-1 only (500 molecules/μm²) or ICAM-1 and OVA–MHC-I (200 molecules/μm²). (Scale bars, 10 μm.) (*Middle*) Molecular density maps from representative regions (4 μm × 4 μm) highlighted in the single-molecule images (red boxes); normalized relative density is pseudocolored according to the depicted scale. (*Bottom*) Zoomed cluster maps (1.5 μm × 1.5 μm) corresponding to red boxes in the *Middle* row. CD3ζ molecules in clusters are colored green and molecules outside clusters are in blue. Cluster contours are highlighted with red lines. (*B*) Cluster maps of representative CD3ζ and pCD3ζ image regions (4 μm × 4 μm) in Jurkat–OT-I cells on activating surfaces as in *A*. (*C*) Relative density in clusters of CD3ζ (ratio of molecular density of CD3ζ inside clusters to total molecular density) for the conditions presented in *A*. Data are mean ± SEM from 7 to 20 regions from 4 to 6 cells per condition; **P < 0.01 and ***P < 0.001 (unpaired *t* test).

and pMHC-I stimulation had different effects for different TCRs with respect to percentage of molecules in clusters, cluster area, number of clusters per area, and cluster shape (*SI Appendix*, Figs. S3 *C—H* and S4). However, there was one cluster parameter that was consistent across different TCRs, namely the molecular density within clusters, which was always significantly higher in activated versus resting T cells irrespective of antibody versus pMHC-I conditions (Fig. 1*C* and *SI Appendix*, Fig. S5). In addition, we found that the longer the stimulation, the denser the CD3ζ clusters became, both for antibody and pMHC stimulation (*SI Appendix*, Fig. S6). Noticeably, pCD3ζ was visibly more clustered than CD3ζ (Fig. 1*B*), which was also reflected in a higher percentage of pCD3ζ molecules in clusters and a higher molecular density of pCD3ζ vs. CD3ζ clusters (*SI Appendix*, Fig. S7). This was not an artifact caused by different photophysical properties of the fluorophores, because pCD3ζ clusters were denser than

TCR–CD3 clusters, even when imaged with the same fluorophore, Alexa Fluor647 (*SI Appendix*, Fig. S7D). Together, these findings suggest a correlation between CD3ζ clustering and CD3ζ phosphorylation.

The Density of CD3ζ Molecules in Clusters Determines Triggering Efficiency. To identify triggered and nontriggered TCR–CD3 complexes within a single-molecule image, we conducted two-color SMLM imaging (Fig. 2*A*) and developed an analysis strategy that combines cluster detection and colocalization analysis. The degree-of-colocalization (DoC) analysis (29) determines the local density for each molecule at increasing radii, providing a density gradient for each channel (Fig. 2*B*). The analysis correlates the two density gradients and assigns a DoC score to each molecule, with −1 being anticorrelated (i.e., the two proteins are segregated), 0 meaning no correlation, and +1 being correlated (i.e., the two proteins are colocalized). We verified that the DoC analysis is: (*i*) insensitive to total or relative expression level in either channel; (*ii*) insensitive to whether colocalized molecules are randomly distributed or clustered; and (*iii*) unaffected by "undetected" molecules (*SI Appendix*, Figs. S8 and S9). When applied to CD3ζ molecules to analyze colocalization with pCD3ζ, this approach allows us to discriminate triggered from nontriggered TCR–CD3 complexes. In T cells stimulated on bilayers with physiological concentrations of pMHC-I (400 molecules/μm²) (Fig. 2*C*), the majority of CD3ζ molecules had a low DoC score. We defined a DoC score threshold of ≥0.4 for colocalization (*SI Appendix*, Fig. S10) and found that only ∼23% of all CD3ζ molecules were colocalized with pCD3ζ (i.e., triggered). Because we retained the spatial information, we could determine the average DoC score for clustered and nonclustered molecules (Fig. 2*D*). Although ∼20% of total CD3ζ molecules resided outside clusters, only 12.5% of these nonclustered CD3ζ molecules had a DoC score ≥0.4 (*SI Appendix*, Fig. S11A), strongly indicating a low triggering efficiency for nonclustered molecules. These triggered nonclustered molecules represent only 18% of all triggered CD3ζ molecules (Fig. 2*F*), whereas the majority (∼80%) of triggered CD3ζ molecules (Fig. 2*F*) resided in clusters that contained 30% of all CD3ζ molecules (Fig. 2*E*). This finding is consistent with the overall higher degree of clustering of pCD3ζ (Fig. 1*B* and *SI Appendix*, Fig. S7).

Closer inspection of the TCR triggering maps (Fig. 2*C*) revealed that some clusters contained predominantly triggered CD3ζ molecules, whereas others contained only nontriggered CD3ζ molecules. To distinguish these two types of clusters, we defined "triggered CD3ζ clusters" as containing ≥10 CD3ζ molecules that have a DoC score ≥0.4 (i.e., containing ≥10 triggered CD3ζ molecules per cluster). This definition was justified because it meant that triggered CD3ζ clusters contained close to 80% of all triggered CD3 molecules, whereas nontriggered clusters contained <5% (Fig. 2*F*). The most striking difference between triggered and nontriggered clusters was the molecular density within clusters; triggered clusters were ∼twofold denser than nontriggered clusters (Fig. 2*G*). This was true for all three TCRs as well as for antibody and pMHC-I activation, thereby indicating generality in our observations (*SI Appendix*, Fig. S11B). Importantly, we confirmed that the presence of endogenous, unlabeled CD3ζ did not bias the analysis, because we obtained the same results
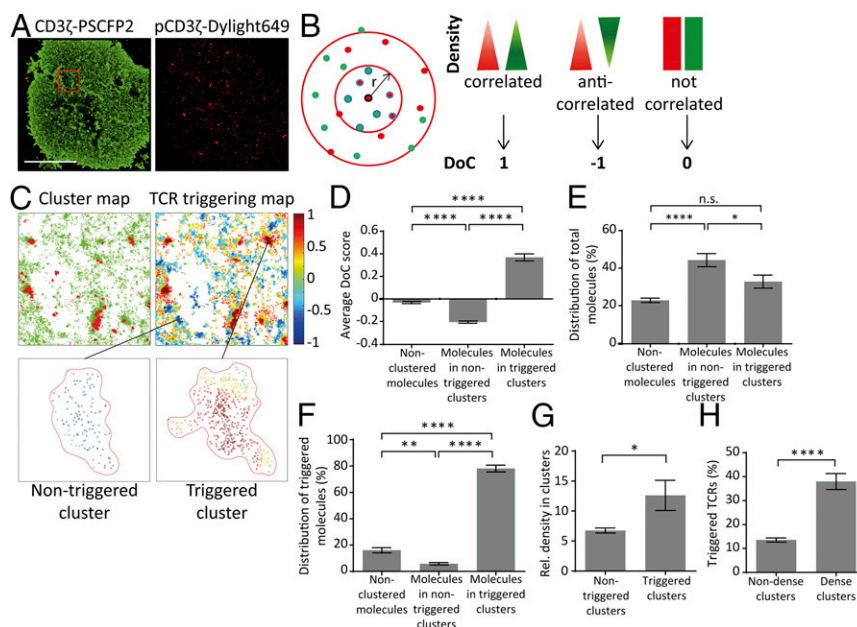

Fig. 2. TCR triggering occurs in dense clusters. (*A*) Two-color single-molecule images of CD3ζ–PSCFP2 (*Left*) and pCD3ζ–Dylight649 (*Right*) in a Jurkat-ILA1 cell stimulated (15 min) on a lipid bilayer presenting ICAM-1 (500 molecules/μm²) and high-affinity 3G–MHC-I (400 molecules/μm²). (Scale bar, 10 μm.) (*B*) DoC analysis. From the molecular coordinates of CD3ζ and pCD3ζ, the local density of each channel is calculated at increasing radius sizes around each molecule, providing density gradients for both channels. The two gradients of density are tested for correlation, resulting in a DoC score for each molecule. DoC scores range from −1 to +1, with −1 indicating segregation, 0 indicating random distribution, and +1 indicating colocalization. (*C*) Cluster map (*Left*) of CD3ζ (green) and pCD3ζ (red), and corresponding pseudocolored DoC map (*Right*), for CD3ζ molecules in the highlighted region in *A* (red box, 4 μm × 4 μm). Black dots in the cluster map represent nonclustered molecules. Below are shown enlarged nontriggered and triggered CD3ζ clusters with molecules color-coded according to their DoC scores. (*D*) Average DoC score of CD3ζ molecules outside clusters, in nontriggered clusters and in triggered clusters. (*E*) Distribution of total CD3ζ molecules between nonclustered molecules, molecules in nontriggered clusters, and molecules in triggered clusters. (*F*) Distribution of triggered CD3ζ molecules between nonclustered molecules, molecules in nontriggered clusters and molecules in triggered clusters. (*G*) Relative density of CD3ζ molecules in triggered and nontriggered clusters. (*H*) The percentage of CD3ζ molecules that are triggered in nondense and dense clusters. Clusters were classified as dense or nondense based on the density threshold defined in *SI Appendix*, Fig. S12. In *D–H*, data are mean ± SEM from 10 regions from 5 cells. In *D–F*, **$P < 0.01$ and ****$P < 0.0001$ (one-way ANOVA). In *G* and *H*, *$P < 0.05$ and ****$P < 0.0001$ (paired t test).

with Jurkat–1G4 cells that lack endogenous, unlabeled CD3ζ (*SI Appendix*, Figs. S2C, S4C, S5 *A* and *B*, S7A, and S11B). For antigen-stimulated Jurkat–ILA1 cells, nontriggered clusters had an average of 3 CD3ζ molecules and a diameter of ~54 nm, corresponding to an average CD3ζ-to-CD3ζ spacing of ~17 nm (3,500 molecules/μm²), whereas triggered clusters had 55 CD3ζ molecules and a diameter of ~185 nm, with an average spacing of ~10 nm (9,500 molecules/μm²) (*SI Appendix*, Fig. S11C).

Given that pMHC-I engagement and antibody stimulation induced the formation of dense TCR–CD3 clusters (Fig. 1C) and triggered CD3ζ resided predominantly in dense clusters (Fig. 2 *F* and *G*), it was also possible to group clusters according to their density (*SI Appendix*, Fig. S12) and demonstrate that dense clusters had a higher TCR triggering efficiency (Fig. 2H). Although only ~30% of CD3ζ resided in dense clusters (*SI Appendix*, Fig. S12B), these molecules constituted the majority of triggered CD3ζ molecules.

TCR Engagement Leads to Receptor Clustering Independently of Phosphorylation.

Although the data show that denser TCR–CD3 clusters have a higher probability of being triggered, it is still unclear whether tighter clustering leads to increased phosphorylation of CD3ζ or whether phosphorylated TCR–CD3 molecules preferentially associate into dense clusters. To investigate this, we used a CD3ζ mutant where all three ITAM sequences in CD3ζ were modified by replacing the two key tyrosine residues in each ITAM with leucine (CD3ζ–6YL) (Fig. 3A). The CD3ζ–6YL mutant was fused to PSCFP2 and imaged in Jurkat–1G4 cells in which expression of endogenous CD3ζ was blocked with CRISPR/Cas9 gene editing. Jurkat–1G4 cells reconstituted with CD3ζ–6YL–PSCFP2 were activated on antibody-coated slides (Fig. 3 *B–E*) or pMHC-I–presenting bilayers (Fig. 3F). We confirmed that CD3ζ could not be phosphorylated in cells expressing only the CD3ζ–6YL mutant (Fig. 3B) and that pZap70 staining was minimal (Fig. 3C).

Cells expressing the CD3ζ–6YL mutant only did not spread on the antibody-coated glass to the same extent as cells expressing wild-type CD3ζ, indicating reduced T-cell activation (Fig. 3D). However, CD3ζ clustering was similar to the wild-type CD3ζ: the CD3ζ–6YL mutant formed denser clusters after T-cell activation with either antibody-coated slides (Fig. 3E) or pMHC-containing bilayers (Fig. 3F) and these CD3ζ–6YL nanoclusters had a similar density than wild-type CD3ζ nanoclusters. Overall, these results suggest that the reorganization of CD3ζ into dense clusters upon TCR engagement was not dependent on the phosphorylation of CD3ζ. Thus, the formation of dense TCR–CD3 nanoclusters may precede CD3 phosphorylation.

Dense TCR–CD3 Clusters Are Signaling-Competent.

In order for a productive signal to be transmitted following ligand binding and TCR–CD3 phosphorylation, downstream signaling molecules such as Zap70 and Lat are recruited to phosphorylated TCR–CD3 complexes and in turn phosphorylated (37). To test the signaling competency of CD3ζ clusters, we examined the colocalization of CD3ζ with phosphorylated Zap70 (pZap70) (Fig. 4A) and phosphorylated Lat (pLat) (Fig. 4B). Irrespective of whether we compared noncolocalized clusters with colocalized clusters (containing ≥10 CD3ζ molecules with a DoC score ≥ 0.4) or nondense clusters with dense clusters (relative molecular density >6), we found that CD3ζ clusters containing downstream signaling molecules were dense and that dense clusters contained more signaling proteins. Thus, the thresholds we defined did not influence the outcome: the molecular density within clusters determined the signaling competency of TCR–CD3 clusters.

We also examined the distribution of Lck and CD45 relative to CD3ζ. Interestingly, although we found that pZap70 and pLat had a large fraction of molecules colocalized with CD3ζ, relatively few Lck molecules colocalized with CD3ζ (Fig. 4C), suggesting that transient Lck–CD3ζ interactions may be sufficient to

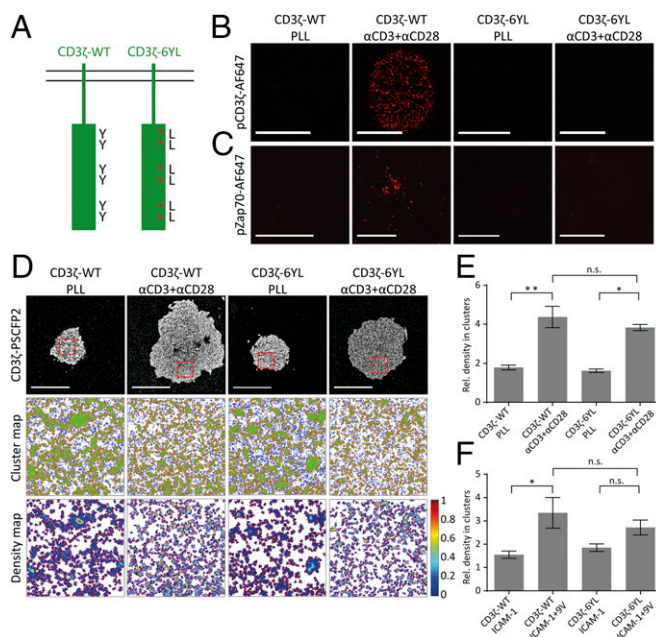**Fig. 3.** CD3ζ clustering occurs independently of phosphorylation. (*A*) Schematic depicting the CD3ζ–6YL mutant in which the tyrosine (Y) residues contained in the ITAM consensus sequences that have been mutated to leucine (L). The CD3ζ–6YL mutant no longer contains any phosphorylation sites. (*B* and *C*) Confocal microscopy images of Jurkat–1G4 cells lacking endogenous CD3ζ that were transfected to express wild-type CD3ζ (CD3ζ–WT) or the CD3ζ–6YL mutant, on PLL or antibody-coated (αCD3+αCD28) glass surfaces and immunostained for (*B*) pCD3ζ or (*C*) pZAP70. (Scale bars, 10 μm.) (*D, Top*) Single-molecule images of CD3ζ–WT–PSCFP2 or CD3ζ–6YL–PSCFP2 in Jurkat–1G4 cells on resting (PLL-coated) or antibody-coated (anti-CD3ε and anti-CD28 antibodies, αCD3+αCD28) glass surfaces. (Scale bars, 10 μm.) (*Middle*) Cluster maps of representative regions (4 μm × 4 μm) highlighted in the single molecule images (red boxes); where CD3ζ molecules in clusters are green and molecules outside clusters are in blue. Cluster contours are highlighted with red lines. (*Bottom*) Corresponding molecular density maps; normalized relative density is pseudocolored according to the depicted scale. (*E* and *F*) Relative density of CD3ζ–WT and CD3ζ–6YL in clusters for Jurkat–1G4 cells (*E*) on PLL- or antibody-coated glass or (*F*) on bilayers containing ICAM-1 only or ICAM-1 and high-affinity 9V–MHC-I. Data are mean ± SEM from 10 to 38 regions from 7 to 13 cells per condition; *P < 0.05; **P < 0.01 (ANOVA).

initiate signaling at TCR signaling "hot spots" (26, 38). More CD3ζ molecules colocalized with Lck at 5 min than at later time points (Fig. 4D), supporting the notion that Lck may depart signaling clusters following early recruitment, resulting in an overall low level of colocalization as previously reported (39, 40). Furthermore, although CD3ζ clusters contained pLat (Fig. 4B), our imaging and analysis approach cannot discriminate between pLat molecules in the plasma membrane and pLat molecules residing in vesicles (25) that are adjacent to the plasma membrane.

CD45 molecules were partially segregated from CD3ζ molecules, as judged by the low level of colocalization between CD45 and CD3ζ (Fig. 4C). The kinetic segregation model proposes that CD45 exclusion initiates and sustains TCR signaling, because it shifts the balance of phosphatase and kinase activity in favor of phosphorylation (41). When we investigated the relative distribution of CD3ζ and CD45 at the nanoscale level, the percentage of CD45 molecules that colocalized with CD3ζ was lower in activated cells than in resting cells, independent of the type of stimulation (Fig. 5 *A–C*). Furthermore, in activated cells, the small fraction of CD45 molecules that did colocalize with CD3ζ molecules were found in nondense clusters and colocalized clusters had a lower molecular density of CD3ζ than noncolocalized clusters (Fig. 5 *D* and *E*). Together, these data support
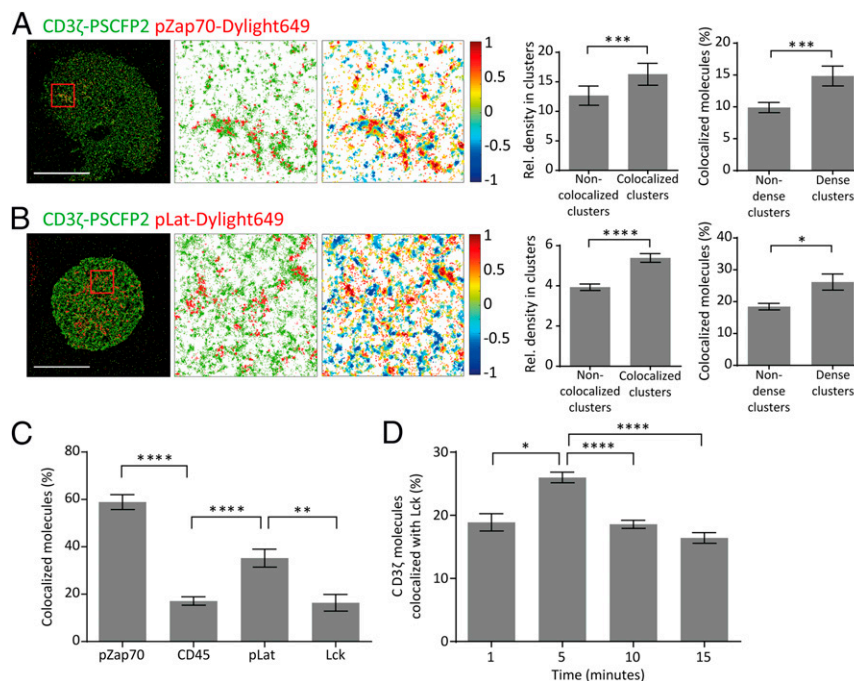
Fig. 4. TCR clustering amplifies recruitment of downstream signaling molecules. (*A* and *B*, *Left*) Two-color single-molecule images and zoomed 4-μm × 4-μm regions of (*A*) CD3ζ and pZap70 and (*B*) CD3ζ and pLat in Jurkat–ILA1 cells stimulated for 15 min on lipid bilayers presenting ICAM-1 (500 molecules/μm²) and 3G–MHC-I (400 molecules/μm²). (Scale bars, 10 μm.) (*Middle*) DoC maps of CD3ζ color-coded according to the DoC with pZap70 or pLat in representative 4-μm × 4-μm regions. (*Right*) Relative density of CD3ζ molecules in colocalized and noncolocalized clusters with pZap70 or pLat. Colocalized clusters contained ≥10 CD3ζ molecules with a DoC score of ≥0.4. (*Far Right*) Percentage of CD3ζ molecules colocalized with pZap70 or pLat in dense and nondense CD3ζ clusters. *$P <$ 0.05, **$P <$ 0.01, ***$P <$ 0.001, and ****$P <$ 0.0001 (paired *t* test). (*C*) Percentage of pZap70, CD45, pLat, and Lck molecules colocalized with CD3ζ. **$P <$ 0.01 and ****$P <$ 0.0001 (ANOVA). (*D*) Percentage of CD3ζ molecules colocalized with Lck in Jurkat–ILA1 cells stimulated on lipid bilayers presenting ICAM-1 (500 molecules/μm²) and 3G-MHC-I (400 molecules/μm²) for different durations (1, 5, 10, and 15 min). *$P <$ 0.05 and ****$P <$ 0.0001 (ANOVA).

that CD45 is excluded selectively from dense TCR–CD3 clusters, possibly because of the large size of the CD45 ectodomain (41), through charge repulsion (19) or through molecular crowding (42).

The Strength of pMHC–TCR Interaction Is Translated into Phosphorylation Levels via the Density of TCR–CD3 Nanoclusters. Given that the molecular density within clusters correlated with TCR–CD3 signaling efficiency, we investigated whether T cells used the pMHC-I–induced formation of dense clusters for antigen discrimination. If ligand binding drives TCR clustering, then ligand affinity and dose should regulate this process. Altered peptide ligands are antigenic peptides containing mutations in the TCR contact site, giving rise to ligands with differences in affinity for the TCR that correlate with downstream signaling potential (43). We used a library of altered peptide ligands for the ILA1 TCR (4) and examined the density of CD3ζ clusters (Fig. 6 *A* and *B*) and T-cell activation (*SI Appendix*, Fig. S13 and S14) in response to pMHC-I molecules with a range of binding affinities (K_D = >500–2.9 μM) at identical densities (~400 molecules/μm²) (Fig. 6*A* and *SI Appendix*, Fig. S13) or with the same binding affinity (K_D = 2.9 μM) at different densities (40–4,000 molecules/μm²) (Fig. 6*B* and *SI Appendix*, Fig. S14). Interestingly, calcium fluxes could be detected in T cells on all bilayers containing pMHC-I molecules (*SI Appendix*, Figs. S13 and S14), suggesting that calcium fluxes may not require pMHC-induced changes in TCR–CD3 clustering. The fraction of cells displaying a dense ring of F-actin at the synapse periphery, an indicator of cell spreading during activation, as well as the average cell area, both increased as a function of pMHC-I affinity and dose, confirming that ligand affinity and density affect the extent of downstream cellular outcomes.

We first characterized CD3ζ nanoclusters and found that the molecular density within CD3ζ nanoclusters depended both on

pMHC-I affinity and concentration (Fig. 6 *A* and *B*). We confirmed that triggered CD3ζ clusters had a higher molecular density than nontriggered clusters (Fig. 6*C*), which resulted in a correlation between the molecular density within CD3ζ clusters and the overall level of CD3ζ phosphorylation (Fig. 6*D*). Hence, the ability of pMHC-I molecules to induce dense CD3ζ clusters was found to be a function of pMHC–TCR affinity and dose and correlated with the amount of signal generated. Given that CD3ζ clustering was independent of CD3ζ phosphorylation (Fig. 3), our data suggest that it is the formation of dense clusters that translates pMHC–TCR interactions into intracellular signals.

To investigate whether TCR–CD3 clustering is a universal mechanism for the translation of pMHC binding into signal initiation, we confirmed the finding in primary mouse OT-I CD8⁺ T cells on bilayers with various pMHC-I densities (Fig. 6*E*). Using immunostaining to probe for TCR-β and pCD3ζ, we found that the density of TCR-β nanoclusters depended on the pMHC-I doses and that triggered clusters had a higher molecular density than nontriggered clusters in primary T cells (Fig. 6*F*). Importantly, the formation of dense clusters under the control of pMHC-I dose strongly correlated with the overall amount of pCD3ζ (Fig. 6*G*). Thus, TCR-β clustering translated pMHC-I dose into the amount of local signal generated. Taken together, our data suggest that pMHC-I–induced spatial reorganization of the TCR–CD3 complex allows T cells to probe for and discriminate antigens.

Discussion

Although all TCR signaling begins with the phosphorylation of the TCR–CD3 complex, how ligand binding to the TCR on the extracellular side initiates phosphorylation of intracellular ITAM domains on CD3 dimers remains a topic of intense debate (1, 2, 16). Combining a cluster detection (28) and colocalization (29)
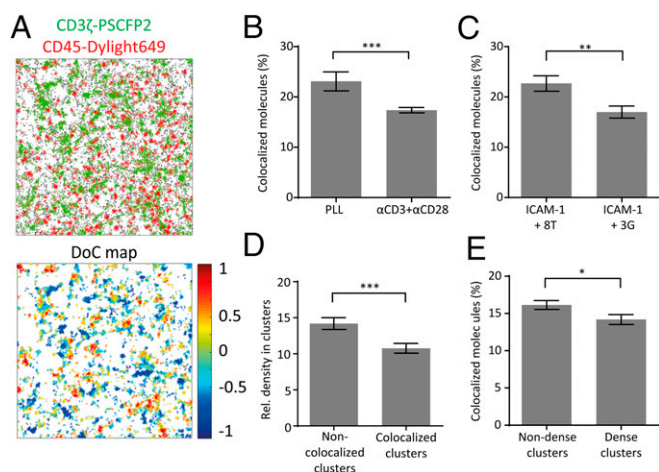
Fig. 5. CD45 is excluded from CD3ζ clusters in activated T cells. (*A*) Two-color single-molecule map (4 μm × 4 μm) of CD3ζ and CD45 in Jurkat–ILA1 cells on antibody-coated (αCD3+αCD28) glass surface (*Upper*) and corresponding DoC map, where CD3ζ molecules are color-coded according to their DoC score (*Lower*). (*B* and *C*) Percentage of CD45 molecules colocalized with CD3ζ in Jurkat–ILA1 cells on resting (PLL-coated) or antibody-coated (anti-CD3ε and anti-CD28 antibodies, αCD3+αCD28) glass surfaces (*B*, 10 min) and on supported lipid bilayers (*C*, 15 min) containing ICAM-1 (500 molecules/μm²) and low-affinity 8T–MHC-I (400 molecules/μm²) or ICAM-1 and high-affinity 3G–MHC-I (400 molecules/μm²). Data are mean ± SEM from 11 to 44 regions from 4 to 10 cells per condition; **P < 0.01 and ***P < 0.001 (unpaired *t* test). (*D*) Relative density of CD3ζ molecules in colocalized and noncolocalized clusters with CD45. Colocalized clusters contained ≥10 CD3ζ molecules with a DoC score of ≥0.4. (*E*) Percentage of CD3ζ molecules colocalized with CD45 in dense and nondense clusters. In (*D* and *E*), data are mean ± SEM from 44 regions from 10 cells; *P < 0.05 and ***P < 0.001 (paired *t* test).

analysis for SMLM data, we demonstrated here that individual TCR–CD3 complexes have different probabilities of being phosphorylated depending on their proximity to neighboring TCR complexes. Our finding places spatial organization at the forefront of the regulation of TCR signaling. Taken together, our data propose the following mechanistic insights of how TCR signaling begins: pMHC–TCR interactions are first translated into TCR–CD3 nanoclusters. The pMHC dose and affinity are reflected in the molecular density within the clusters. Therefore, in this first step, the antigen recognition event is converted into a spatial pattern. The second step translates the spatial pattern: that is, the density within the TCR–CD3 nanoclusters back into a biochemical signature (i.e., the amount of TCR–CD3 phosphorylation). This finding means that the overall signal generated mirrors the binding characteristics of the pMHC–TCR interaction.

Given TCR diversity and MHC polymorphisms and therefore the plethora of pMHC–TCR interactions (44), it is not surprising that no common spatial arrangement of the TCR–CD3 complex exists in resting or activated T cells. Thus, our data may reconcile the seemingly contradictory reports of TCR–CD3 monomers (45), functional dimers (46), clusters (47–49), and protein islands (23). The diversity in TCR–CD3 nanocluster characteristics is, however, intriguing. Remodeling of these clusters would allow T cells to set activation thresholds (4), for example by preclustering TCRs (48, 49) or restructuring cortical actin (50), to enhance or prevent pMHC-induced clustering of TCRs.

A corollary of placing TCR–CD3 clustering after pMHC engagement and before signal initiation is that signaling should spontaneously begin in dense TCR–CD3 nanoclusters. This finding is consistent with models, such as the kinetic segregation model (41), which proposes that TCR signaling does not require the activation of kinases (51) but only the exclusion of phosphatases,

such as CD45 from the TCR. Exclusion could be driven by the large size of CD45 ectodomains that cannot be accommodated within the limited space between the antigen-presenting cell membrane and the T-cell membrane (41) or simply by charge repulsion (19) or molecular crowding (42). Indeed, we observed a selective reduction of CD45 in dense TCR–CD3 nanoclusters but found no evidence for the recruitment of Lck to these clusters. Whether shifting the balance of phosphatases to kinases within and around nanoclusters is sufficient remains to be seen.

A striking feature in our data is that the molecular density within TCR–CD3 correlated with signaling efficiency. The average spacing between CD3ζ molecules decreased from 17 nm in nontriggered clusters to 10 nm in triggered clusters. It is thus possible that there is cooperativity between TCRs in clusters, either through transmission of conformational changes to neighboring
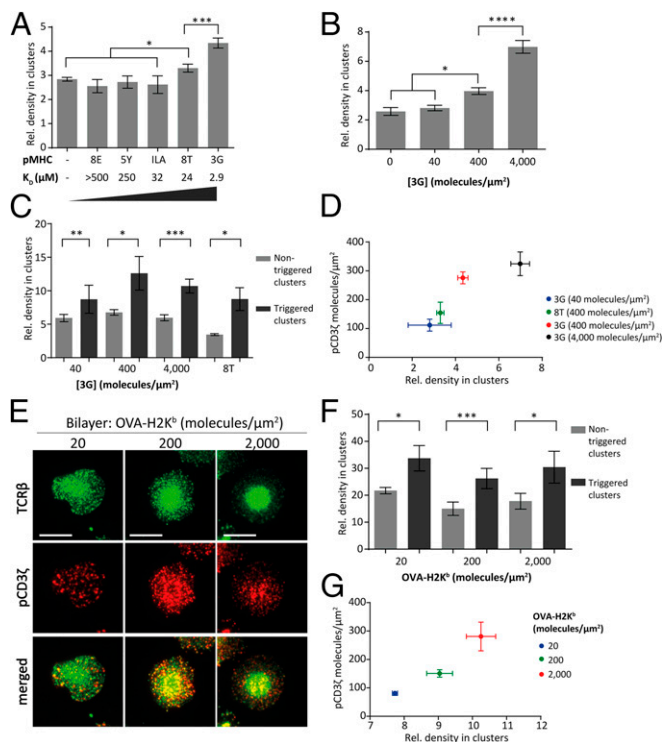

Fig. 6. TCR triggering efficiency as a function of pMHC affinity and concentration. (*A* and *B*) Relative density of CD3ζ molecules in clusters in Jurkat–ILA1 cells on lipid bilayers (15 min) presenting (*A*) ICAM-1 (500 molecules/μm²) and pMHC-I (400 molecules/μm²) of different affinities (K_D ranging from >500 μM to 2.9 μM) or (*B*) ICAM-1 (500 molecules/μm²) and high-affinity 3G–MHC-I (K_D = 2.9 μM) at different concentrations (40–4,000 molecules/μm²). Data are mean ± SEM from 6 to 30 regions from 3 to 11 cells per condition. *P < 0.05, ***P < 0.001, and ****P < 0.0001 (one-way ANOVA). (*C*) Relative density of CD3ζ molecules in triggered and nontriggered clusters in Jurkat–ILA1 cells on bilayers with 3G–MHC-I (K_D = 2.9 μM) at 40, 400, and 4,000 molecules/μm² and 8T–MHC-I (K_D = 24 μM) at 400 molecules/μm². (*D*) Number of pCD3ζ molecules/μm² detected in Jurkat–ILA1 cells stimulated as in *C* as a function of the relative density of CD3ζ in clusters. In *C* and *D*, data are mean ± SEM from at least nine regions from three cells per condition. *P < 0.05, **P < 0.01, and ***P < 0.001 (paired *t* test for *C*). (*E*) TIRF images of TCR-β (green) and pCD3ζ (red) in primary mouse OT-I CD8⁺ T cells stimulated for 10 min on lipid bilayers with ICAM-1 (500 molecules/μm²), B7.1 and different OVA–MHC-I densities (20, 200, or 2,000 molecules/μm²). (Scale bars, 10 μm.) (*F*) Relative density of TCR-β molecules in triggered and nontriggered clusters in primary mouse OT-I CD8⁺ T cells stimulated as in *E* and imaged by two-color dSTORM. (*G*) Number of pCD3ζ molecules/μm² for conditions shown in *F* as a function of the relative density of CD3ζ in clusters. For *F* and *G*, data are mean ± SEM from 7 to 10 regions from 4 to 5 cells per condition. *P < 0.05 and ***P < 0.001 (paired *t* test for *F*).

TCRs (52) or through increased localized phosphorylation of TCRs by clustered Lck (26, 27). Signaling efficiency in dense clusters may also be augmented by the detachment of the ITAM-containing cytoplasmic domains of CD3ζ (53) and CD3ε (54) from the membrane so that they are accessible to Lck for phosphorylation. This so-called safety-lock mechanism of TCR signaling could be overcome in densely packed nanoclusters. Similarly, the stabilizing influence of neighboring TCRs could effectively prolong TCR–pMHC-I interactions (48, 55) and the immobilization of clustered TCRs (23) could enable multiple rounds of rebinding (56) and serial engagements (57, 58). All of these processes including CD45 exclusion could contribute to the enhanced signaling competency of densely packed TCR–CD3 nanoclusters.

Our data demonstrated that CD3ζ clustering upon antibody and pMHC stimulation did not require CD3ζ phosphorylation, strongly suggesting that clustering precedes phosphorylation. In agreement with the notion that clustering drives signaling, rather than phosphorylation leading to clustering, artificial clustering of CD3ζ using a chemically inducible system resulted in strong TCR–CD3 phosphorylation under physiological levels of Lck and CD45 (59). Taking these data together, we find that it is indeed possible that signaling begins spontaneously in dense TCR–CD3 clusters.

Why would an intermediate step between pMHC engagement and signal initiation be beneficial to T cells? To explain how TCR triggering accounts for the selectivity, specificity and speed of the T-cell response (1), mathematical models have linked "input" (e.g., pMHC dose and TCR–pMHC affinity) to "output" (e.g., signaling and cytokine secretion) (60). The kinetic proofreading model (61), for example, proposed that the TCR needs to undergo a series of intermediate steps before being triggered so that the overall response depends on the TCR–pMHC dissociation time. Other models propose an optimal dwell time for TCR–pMHC interactions (62) or serial engagement of different TCRs by the same pMHC (57, 63). In all of these models, the intermediate steps are necessary for antigen discrimination. We propose here that the pMHC-induced formation of TCR–CD3 nanoclusters is the intermediate step that allows T cells to distinguish both pMHC binding affinity and dose. Spatial reorganization could explain how structurally and biophysically diverse TCR–pMHC interactions result in a common TCR triggering mechanism.

The mechanisms underlying the formation, regulation, and reorganization of TCR nanoclusters remain unclear and represent a major area of interest for future research. Previous studies have suggested that the actin cytoskeleton might be involved in the formation of TCR microclusters (39) and in the regulation of T-cell signaling clusters (19). In resting cells, the nonrandom distribution of the TCR may be maintained by cytoskeleton-based partitioning of the membrane into domains (64). TCR/pMHC binding occurs in regions of close contact and the increased TCR cluster density observed in activated T cells may represent the consolidation of these close contact regions driven by minimization of membrane bending energy (42). Another possibility is that pulling induces a conformational change in the structure of the TCR–CD3 complex that would favor the clustering of engaged TCR–CD3 complexes with other unengaged TCR–CD3 complexes. There is mounting evidence that mechanical forces are at play in the processes of TCR triggering and antigen discrimination (1, 65), but other mechanisms may also be involved.

In conclusion, the TCR–CD3 complex is not an autonomous signaling unit. Instead, TCR triggering efficiency is dictated by the spacing to neighboring TCR–CD3 complexes. Furthermore, the coupling of ligand binding to signal initiation via spatial reorganization is a process that enables antigen discrimination. Ligand-induced, nanoscale reorganization may also regulate the

signaling efficiencies of other receptor systems and our study provides an experimental and conceptual framework that links spatial organization of individual molecules to their biochemical activity.

Methods

Cell Lines, pMHC Monomers, and Recombinant Proteins. Jurkat T cells (Clone E6.1, ATCC) and other Jurkat-derived cell lines were maintained in RPMI 1640 (Gibco) supplemented with 10% (vol/vol) FCS, 2 mM L-glutamine, and 1 mM penicillin and streptomycin (all from Invitrogen). Cells were transfected by electroporation (NEON; Invitrogen) to express CD3ζ fused to PSCFP2. PSCFP expression construct was from Evrogen.

The ILA1 TCR recognizes residues 540–548 (ILAKFLHWL, abbreviated as ILA) of the human telomerase reverse-transcriptase protein, presented in the context of the human MHC class I HLA-A*0201 (HLA-A2). Jurkat cells stably expressing the ILA1 TCR (called Jurkat–ILA1 hereafter), as well as monomeric human HLA-A2 complexed with the ILA peptide and several altered peptides (3G, 8T, 5Y, 8E) were used in this study. These peptide ligands have been characterized previously (31, 66, 67). Their K_D values are as follows: 3G (2.9 μM), 8T (24 μM), ILA (32 μM), 5Y (250 μM), and 8E (>500 μM).

The 1G4 TCR recognizes the SLLMWITQC peptide presented by HLA-A2 (32, 68). TCR-deficient Jurkat-76 cells were engineered to stably express the 1G4 TCR, and endogenous CD3ζ was knocked out or fused to PSCFP2 by CRISPR/Cas9 technology. Biotinylated pMHC monomers of different affinities were used: 4D (K_D = 252 μM), 6V (K_D = 18 μM), and 9V (K_D = 7.2 μM).

Jurkat-76 cells stably expressing OT-I TCR (called Jurkat–OT-I hereafter) were generated by retroviral transduction. For this, the packaging cell line Phoenix amphotropic (Nolan Laboratory, Stanford University, Stanford, CA) was transfected with Lipofectamine LTX (Invitrogen) with the retroviral plasmid encoding OT-I TCR (TCRa-V2 and TCRb-V5), a gift from Ian Parish, Australian National University, Canberra, ACT, Australia. Viral supernatant collected 24 and 48 h after transfection was used for infection of Jurkat-76 cells. One week after infection, cells expressing OT-I were enriched by flow cytometry. Monomeric mouse H-2K^b complexed with the ovalbumin-derived peptide SIINFEKL (amino acids 257–264) was synthesized at the Australian Cancer Research Foundation Biomolecular Resource Facility at The John Curtin School of Medical Research, Australian National University, using BirA enzyme synthesized as described previously (69). This pMHC was synthesized with a carboxyl-terminal biotin-tag at the α-chain for incorporation on lipid bilayers.

Soluble ICAM-1 recombinant protein with a C-terminal His-tag was produced from stably transfected Schneider cells (S2). Protein production in S2 cells was induced by 0.5 mM CuSO₄ for 5 d. The supernatant containing ICAM-1 was collected by centrifugation, then filtered and dialyzed against PBS plus 1 mM EDTA and then PBS only to remove CuSO₄. ICAM-1 was purified using a 5 mL NiNTA column. His-tagged CD80 recombinant mouse protein (B7.1) was purchased from Life Technologies (50446-M08H-50). Monomeric biotinylated pMHCs and recombinant proteins were stored at −80 °C. Stock dilutions were stored at 4 °C and used for several experiments.

Generation of CD3ζ–6YL Mutant. The CD3ζ–ITAM Tyr to Leu mutant (CD3ζ –6YL) was generated by consecutive site-directed mutagenesis using the appropriate primer pairs. Mutagenesis at the correct sites was verified by Sanger sequencing.

Primary Mouse OT-I CD8⁺ T Cells. All primary T-cell experiments were approved by the University of New South Wales Animal Care and Ethics Committee. OT-I transgenic mice were bred at Australian BioResources Pty Ltd and were allowed to acclimatize for one week on arrival at the University of New South Wales under specific pathogen-free conditions with a 12-h light/12-h dark cycle before being killed for any experiments.

A single-cell suspension was created by passing a freshly excised spleen through a 40-μm cell strainer (BD Biosciences). Splenocytes were then centrifuged for 5 min at 300 × g and resuspended in 1 mL of red blood cell lysing buffer (Sigma) with gentle mixing for 1 min. Splenocytes were then diluted with 15 mL of PBS, again centrifuged, and resuspended in 10 mL of complete RPMI-1640 culture medium [10% (vol/vol) FBS, 2 mM L-glutamine, 100 μg/mL penicillin and streptomycin, 1 mM sodium pyruvate, 0.1 mM MEM nonessential amino acids, and 0.05 mM 2-Mercaptoethanol]. Cells were then filtered through a 40-μm cell strainer, a viable cell count performed, and 20 × 10⁶ cells cultured in a 75-cm² flask in complete RPMI-1640 for 4 d in the presence of 1 μg OVA₂₅₇₋₂₆₄ (SIINFEKL) peptide (Invivogen), 10 U/mL recombinant murine IL-2 (Peprotech), and 0.03 μg/mL lipopolysaccharides from *Escherichia coli* (0111:B4, Sigma). On day 4, the purity of the preparation was

analyzed by flow cytometry and the cytotoxic T lymphocytes harvested for imaging experiments.

Bilayer Preparation. Glass coverslips (Lab-Tek chambers, 155411, Nunc) were cleaned with 10 M NaOH for 15 min followed by 5 min in 70% (vol/vol) ethanol, then rinsed thoroughly with MilliQ water. A liposome solution of 1 mg/mL with a lipid ratio of 96.5% DOPC, 2% DGS-NTA(Ni), 1% Biotinyl-cap-PE, and 0.5% PEG5,000-PE (mol %; all from Avanti Polar Lipids) was created by vesicle extrusion, as described in detail elsewhere (70). Wells were incubated with liposomes at 0.2 mg/mL for 30 min at room temperature, washed with excess PBS, and blocked with 1% BSA in PBS for 30 min at room temperature. For addition of proteins, bilayers were incubated with 2 μg/mL strep-tavidin (Sigma) for 10 min at room temperature, then washed thoroughly before adding (biotinylated) pMHC (2.5–500 ng/mL) and (His-tagged) ICAM-1 (200 ng/mL) for 100 min at room temperature and thoroughly washing off any excess unbound protein with PBS. Bilayers were loaded with pMHC at a density of 400 molecules/μm^2, unless described otherwise. For experiments with primary mouse cells, the bilayers were also loaded with His-tagged B7.1/CD80 (500 ng/mL). The fluidity of lipids (using rhodamine-labeled DOPE) and proteins (using fluorescent streptavidin) in supported lipid bilayers was assessed by fluorescence recovery after photobleaching (FRAP) on a confocal fluorescence microscope (Fluoview FV1000, Olympus) with a 100× oil-immersion objective with a numerical aperture (NA) of 1.4. The concentration of pMHC on the bilayers was determined by fluorescence correlation spectroscopy (FCS) on a confocal fluorescence microscope (MicroTime200, PicoQuant) with a 100× water-immersion objective with 1.25 NA.

Sample Preparation. For imaging of resting cells, cells were incubated for 10 min at 37 °C on glass surfaces coated with PLL, prepared by incubation of glass coverslips for 30 min at room temperature with 0.01% (wt/vol) PLL (Sigma). For activating cells on glass, cells were allowed to settle on coverslips coated with anti-CD3ε (16-0037; eBioscience) and anti-CD28 (16-0289; eBioscience) for 10 min at 37 °C. Antibodies were adsorbed onto surfaces by incubation of clean glass coverslips with antibody (10-μg/mL each) for at least 1 h at 37 °C. For stimulating cells on lipid bilayers, cells were allowed to settle on bilayers for 10 or 15 mins at 37 °C. Cells were fixed with 4% paraformaldehyde (vol/vol) in PBS for 20 min at room temperature.

For immunostaining, cells were labeled with primary antibody followed by DyLight649- or Alexa Fluor647-conjugated goat antibody specific to the rabbit F(ab′)2 fragment [111-495-047 (discontinued) and 111–606-047; Jackson ImmunoResearch]. Primary antibodies used in this study were against human CD3ζ phosphorylated at Tyr142 either unconjugated (ab68235; Abcam) or directly conjugated to Alexa Fluor647 (558489, BD Biosciences), CD45 (ab10559; Abcam), Lat phosphorylated at Tyr171 (3581S, Cell Signaling), Zap70 phosphorylated at Tyr319 (2701S, Cell Signaling), or Lck (sc-433, Santa Cruz Biotechnology). For experiments with primary mouse cells, an antibody against mouse TCR-β directly conjugated to Alexa Fluor488 or Alexa Fluor647 (H57-597; 109215 and 109218, Biolegend) was used. After fixation, cells were permeabilized with 0.1% (vol/vol) Triton X-100 for 4 min at room temperature, blocked in 5% BSA (wt/vol) in PBS, and probed for 1 h at room temperature with primary and secondary antibodies sequentially. An oxygen-scavenging PBS-based buffer (containing 25 mM Hepes, 25 mM glucose, 5% (vol/vol) glycerol, 0.05 mg/mL glucose oxidase, and 0.025 mg/mL horse-radish peroxidase, supplemented with 50 mM cysteamine; all from Sigma) was used for dSTORM imaging.

Imaging Calcium Fluxes and Actin Polymerization. For imaging calcium fluxes and actin polymerization in response to different conditions, cells were imaged by confocal microscopy using an SP5 inverted confocal microscope (TCS SP5 WLL STED; Leica Microsystems) using a 20× or 63× water-immersion objective (NA = 1.2). For visualization of calcium fluxes, cells were treated with 5 μM Fluo-4-AM (Life Technologies) for 1 h at room temperature. Cells were washed twice and resuspended in HBSS, then imaged live as they were landing on bilayers. For imaging actin polymerization, cells were stained with phalloidin conjugated to Alexa Fluor488 (Life Technologies) for 1 h at room temperature. For both Fluo-4-AM and phalloidin-AF488, the fluorescence signal was visualized using the 488-nm laser line (fluorescence was collected between 500 and 575 nm). Data analysis and processing were performed using ImageJ software (National Institutes of Health). For analysis of calcium flux data, the number of responding cells was quantified and the "cell activation time" (i.e., the duration between the cell landing on the surface and the increase in Fluo-4-AM signal) was measured for cells in which a calcium flux was detected. For analysis of cell spreading, the number of spread cells was quantified and the cell area was measured for all cells based on a thresholded image of the phalloidin staining. Spreading of cells was

defined by the presence of a polymerized "actin ring" (i.e., a broad ring of intense F-actin staining surrounding an unstained cell center).

Single-Molecule Localization Microscopy. PALM and dSTORM image sequences were acquired on a total internal reflection fluorescence (TIRF) microscope (ELYRA, Zeiss) with a 100× oil-immersion objective (NA = 1.46). Photo-conversion of PSCFP2 was achieved with 8 μW of 405-nm laser radiation and the green-converted PSCFP2 was imaged with 18 mW of 488-nm light. For DyLight649/Alexa Fluor647 dSTORM, 15 mW of 633-nm laser illumination was used for imaging, with 0.1–1 mW of 488 nm for conversion from the dark state. For PALM and dSTORM, 20,000 images were acquired per sample with a cooled, electron-multiplying charge-coupled device camera (iXon DU-897; Andor) with an exposure time of 30 ms. For two-color acquisitions, the DyLight649/Alexa Fluor647 channel was acquired first, followed by PSCFP2. Raw fluorescence intensity images were analyzed with the software Zen 2011 SP3 (Zeiss MicroImaging), generating tables containing the *x-y* particle coordinates of each molecule detected in the acquisition.

Cluster Analysis of One-Color Data. SMLM data were analyzed using custom software written in MATLAB (MathWorks) for detection of clusters and extraction of clustering parameters. Typically, for each cell one to five non-overlapping representative regions of 4 × 4 μm^2 were selected for analysis.

First we used Ripley's K function (71) to determine the extent of clustering of a population of molecules compared with a randomly distributed set of molecules. This amount was calculated using SpPack, an add-in for Microsoft Excel (72), as well as a custom MATLAB version optimized for larger datasets. In short, the Ripley's K function calculates for each molecule the number of neighbor molecules within a given radius r corrected by the total density; finally, for each radius the average is calculated over all molecules. The Ripley's K function provides ensemble information on the whole region of interest; it provides information on the level of clustering of molecules in a region. However no analysis is performed at the cluster level and therefore no information is available on individual clusters.

To retrieve information on individual clusters, we used DBSCAN analysis (28) to identify individual clusters. The DBSCAN method detects clusters using a propagative method which links points belonging to the same cluster based on two parameters; the minimum number of neighbors ε (ε = 3) in the radius r (r = 20 nm). The DBSCAN routine was implemented in MATLAB and subsequently coded in c++ and compiled in a MEX file (Matlab executable file) to improve the speed of processing as we are working with large data files.

Two-Color Colocalization Analysis. The two-color data were analyzed using a modified version of the coordinate-based colocalization method (29). The first step in the analysis is to remove molecules which are isolated, by excluding points with a local density below a random distribution (total density = total number of molecules/total area of region of interest). This is important to reduce the size of the dataset because the subsequent steps are highly computationally demanding. In addition, these outlier molecules do not contribute to the clusters and would anyway get excluded in the DBSCAN step.

Then, for each molecule, the local density of each channel is calculated at increasing radius size (10–500 nm), providing the density gradient around that molecule for each channel. The two density gradients are tested for correlation with the Spearman criteria, which score monotonic dependence. This parameter of correlation is corrected with nearest-neighbor distance to account for long distance interactions. As a result, each molecule is scored with this parameter, indicating the DoC, ranging from −1 to 1, with −1 characterizing anticolocalization (or segregation), 0 corresponding to single species, and 1 defining high colocalization. The method favors molecules in clusters compared with randomly distributed molecules. *SI Appendix*, Fig. S9 shows that paired randomly distributed molecules score a lower DoC than clustered molecules independently for paired and unpaired.

From the local density of each molecule taken at a radius of 20 nm and normalized to the total density of the region, a pseudomap is created in which each molecule is represented with a color code corresponding to the normalized density. In a similar way, a map showing the DoC for each molecule is created. These maps enable us to visualize the morphology of the clusters and their organization. The threshold value of 0.4 was determined from simulations to discriminate colocalized from noncolocalized molecules.

In the next step, we detect the individual clusters using a DBSCAN analysis, similarly to the one-color analysis. The clusters are subsequently separated into colocalized clusters (containing more than 10 molecules with a DoC score above 0.4) and noncolocalized clusters. These two populations of clusters are then analyzed to extract their density, size, circularity, and any other type of information.

Statistical Analysis. All statistical analysis was performed using GraphPad software (Prism). Statistical significance between datasets was determined by performing two-tailed, unpaired Student's t tests. For comparing triggered and nontriggered or colocalized and noncolocalized clusters, a paired Student's t test was used. Multiple means were compared with one-way ANOVA and Tukey's multiple comparisons test. Graphs show mean values, and error bars represent the SEM. In statistical analysis, $P > 0.05$ is indicated as not significant (n.s.), whereas statistically significant values are indicated by asterisks as follows: $*P \leq 0.05$, $**P < 0.01$, $***P < 0.001$, and $****P < 0.0001$.

1. van der Merwe PA, Dushek O (2011) Mechanisms for T cell receptor triggering. *Nat Rev Immunol* 11(1):47–55.
2. Chakraborty AK, Weiss A (2014) Insights into the initiation of TCR signaling. *Nat Immunol* 15(9):798–807.
3. Dustin ML, Depoil D (2011) New insights into the T cell synapse from single molecule techniques. *Nat Rev Immunol* 11(10):672–684.
4. van den Berg HA, et al. (2013) Cellular-level versus receptor-level response threshold hierarchies in T-cell activation. *Front Immunol* 4:250.
5. Huppa JB, Davis MM (2003) T-cell-antigen recognition and the immunological synapse. *Nat Rev Immunol* 3(12):973–983.
6. Germain RN, Stefanová I (1999) The dynamics of T cell receptor signaling: Complex orchestration and the key roles of tempo and cooperation. *Annu Rev Immunol* 17:467–522.
7. Sykulev Y, Joo M, Vturina I, Tsomides TJ, Eisen HN (1996) Evidence that a single peptide-MHC complex on a target cell can elicit a cytolytic T cell response. *Immunity* 4(6):565–571.
8. Ma Z, Sharp KA, Janmey PA, Finkel TH (2008) Surface-anchored monomeric agonist pMHCs alone trigger TCR with high sensitivity. *PLoS Biol* 6(2):e43.
9. Huang J, et al. (2013) A single peptide-major histocompatibility complex ligand triggers digital cytokine secretion in CD4(+) T cells. *Immunity* 39(5):846–857.
10. Birnbaum ME, et al. (2014) Molecular architecture of the αβ T cell receptor-CD3 complex. *Proc Natl Acad Sci USA* 111(49):17576–17581.
11. Yokosuka T, et al. (2005) Newly generated T cell receptor microclusters initiate and sustain T cell activation by recruitment of Zap70 and SLP-76. *Nat Immunol* 6(12):1253–1262.
12. Guy CS, et al. (2013) Distinct TCR signaling pathways drive proliferation and cytokine production in T cells. *Nat Immunol* 14(3):262–270.
13. Holst J, et al. (2008) Scalable signaling mediated by T cell antigen receptor-CD3 ITAMs ensures effective negative selection and prevents autoimmunity. *Nat Immunol* 9(6):658–666.
14. Anderson AC, et al. (2005) The Notch regulator Numb links the Notch and TCR signaling pathways. *J Immunol* 174(2):890–897.
15. Roncagalli R, Mingueneau M, Grégoire C, Malissen M, Malissen B (2010) LAT signaling pathology: An "autoimmune" condition without T cell self-reactivity. *Trends Immunol* 31(7):253–259.
16. Kuhns MS, Davis MM (2012) TCR signaling emerges from the sum of many parts. *Front Immunol* 3:159.
17. Grakoui A, et al. (1999) The immunological synapse: A molecular machine controlling T cell activation. *Science* 285(5425):221–227.
18. Monks CR, Freiberg BA, Kupfer H, Sciaky N, Kupfer A (1998) Three-dimensional segregation of supramolecular activation clusters in T cells. *Nature* 395(6697):82–86.
19. Su X, et al. (2016) Phase separation of signaling molecules promotes T cell receptor signal transduction. *Science* 352(6285):595–599.
20. Rossy J, Pageon SV, Davis DM, Gaus K (2013) Super-resolution microscopy of the immunological synapse. *Curr Opin Immunol* 25(3):307–312.
21. Betzig E, et al. (2006) Imaging intracellular fluorescent proteins at nanometer resolution. *Science* 313(5793):1642–1645.
22. Rust MJ, Bates M, Zhuang X (2006) Sub-diffraction-limit imaging by stochastic optical reconstruction microscopy (STORM). *Nat Methods* 3(10):793–795.
23. Lillemeier BF, et al. (2010) TCR and Lat are expressed on separate protein islands on T cell membranes and concatenate during activation. *Nat Immunol* 11(1):90–96.
24. Sherman E, et al. (2011) Functional nanoscale organization of signaling molecules downstream of the T cell antigen receptor. *Immunity* 35(5):705–720.
25. Williamson DJ, et al. (2011) Pre-existing clusters of the adaptor Lat do not participate in early T cell signaling events. *Nat Immunol* 12(7):655–662.
26. Rossy J, Owen DM, Williamson DJ, Yang Z, Gaus K (2013) Conformational states of the kinase Lck regulate clustering in early T cell signaling. *Nat Immunol* 14(1):82–89.
27. Neve-Oz Y, Razvag Y, Sajman J, Sherman E (2015) Mechanisms of localized activation of the T cell antigen receptor inside clusters. *Biochim Biophys Acta* 1853(4):810–821.
28. Ester M, Kriegel H-P, Sander J, Xu X (1996) A density-based algorithm for discovering clusters in large spatial databases with noise. *Knowledge, Discovery and Data Mining, Proceedings* 96(34):pp 226–231.
29. Malkusch S, et al. (2012) Coordinate-based colocalization analysis of single-molecule localization microscopy data. *Histochem Cell Biol* 137(1):1–10.
30. Weissman AM, et al. (1989) Role of the zeta chain in the expression of the T cell antigen receptor: Genetic reconstitution studies. *EMBO J* 8(12):3651–3656.
31. Laugel B, et al. (2007) Different T cell receptor affinity thresholds and CD8 coreceptor dependence govern cytotoxic T lymphocyte activation and tetramer binding properties. *J Biol Chem* 282(33):23799–23810.
32. Jäger E, et al. (1998) Simultaneous humoral and cellular immune response against cancer-testis antigen NY-ESO-1: Definition of human histocompatibility leukocyte antigen (HLA)-A2-binding peptide epitopes. *J Exp Med* 187(2):265–270.
33. Hogquist KA, et al. (1994) T cell receptor antagonist peptides induce positive selection. *Cell* 76(1):17–27.
34. Varma R, Campi G, Yokosuka T, Saito T, Dustin ML (2006) T cell receptor-proximal signals are sustained in peripheral microclusters and terminated in the central supramolecular activation cluster. *Immunity* 25(1):117–127.
35. Heilemann M, et al. (2008) Subdiffraction-resolution fluorescence imaging with conventional fluorescent probes. *Angew Chem Int Ed Engl* 47(33):6172–6176.
36. Owen DM, et al. (2010) PALM imaging and cluster analysis of protein heterogeneity at the cell surface. *J Biophotonics* 3(7):446–454.
37. Hatada MH, et al. (1995) Molecular basis for interaction of the protein tyrosine kinase ZAP-70 with the T-cell receptor. *Nature* 377(6544):32–38.
38. Casas J, et al. (2014) Ligand-engaged TCR is triggered by Lck not associated with CD8 coreceptor. *Nat Commun* 5:5624.
39. Campi G, Varma R, Dustin ML (2005) Actin and agonist MHC-peptide complex-dependent T cell receptor microclusters as scaffolds for signaling. *J Exp Med* 202(8):1031–1036.
40. Roh K-H, Lillemeier BF, Wang F, Davis MM (2015) The coreceptor CD4 is expressed in distinct nanoclusters and does not colocalize with T-cell receptor and active protein tyrosine kinase p56lck. *Proc Natl Acad Sci USA* 112(13):E1604–E1613.
41. Davis SJ, van der Merwe PA (2006) The kinetic-segregation model: TCR triggering and beyond. *Nat Immunol* 7(8):803–809.
42. James JR, Vale RD (2012) Biophysical mechanism of T-cell receptor triggering in a reconstituted system. *Nature* 487(7405):64–69.
43. Sloan-Lancaster J, Allen PM (1996) Altered peptide ligand-induced partial T cell activation: Molecular mechanisms and role in T cell biology. *Annu Rev Immunol* 14:1–27.
44. Rudolph MG, Stanfield RL, Wilson IA (2006) How TCRs bind MHCs, peptides, and coreceptors. *Annu Rev Immunol* 24:419–466.
45. James JR, et al. (2007) Single-molecule level analysis of the subunit composition of the T cell receptor on live T cells. *Proc Natl Acad Sci USA* 104(45):17662–17667.
46. Kuhns MS, et al. (2010) Evidence for a functional sidedness to the alphabetaTCR. *Proc Natl Acad Sci USA* 107(11):5094–5099.
47. Purtic B, Pitcher LA, van Oers NS, Wülfing C (2005) T cell receptor (TCR) clustering in the immunological synapse integrates TCR and costimulatory signaling in selected T cells. *Proc Natl Acad Sci USA* 102(8):2904–2909.
48. Kumar R, et al. (2011) Increased sensitivity of antigen-experienced T cells through the enrichment of oligomeric T cell receptor complexes. *Immunity* 35(3):375–387.
49. Schamel WWA, et al. (2005) Coexistence of multivalent and monovalent TCRs explains high sensitivity and wide range of response. *J Exp Med* 202(4):493–503.
50. Kaizuka Y, Douglass AD, Varma R, Dustin ML, Vale RD (2007) Mechanisms for segregating T cell receptor and adhesion molecules during immunological synapse formation in Jurkat T cells. *Proc Natl Acad Sci USA* 104(51):20296–20301.
51. Nika K, et al. (2010) Constitutively active Lck kinase in T cells drives antigen receptor signal transduction. *Immunity* 32(6):766–777.
52. Minguet S, Swamy M, Alarcón B, Luescher IF, Schamel WW (2007) Full activation of the T cell receptor requires both clustering and conformational changes at CD3. *Immunity* 26(1):43–54.
53. Zhang H, Cordoba S-P, Dushek O, van der Merwe PA (2011) Basic residues in the T-cell receptor ζ cytoplasmic domain mediate membrane association and modulate signaling. *Proc Natl Acad Sci USA* 108(48):19323–19328.
54. Xu C, et al. (2008) Regulation of T cell receptor activation by dynamic membrane binding of the CD3epsilon cytoplasmic tyrosine-based motif. *Cell* 135(4):702–713.
55. Martínez-Martín N, et al. (2009) Cooperativity between T cell receptor complexes revealed by conformational mutants of CD3epsilon. *Sci Signal* 2(83):ra43.
56. Aleksic M, et al. (2010) Dependence of T cell antigen recognition on T cell receptor-peptide MHC confinement time. *Immunity* 32(2):163–174.
57. Valitutti S, Müller S, Cella M, Padovan E, Lanzavecchia A (1995) Serial triggering of many T-cell receptors by a few peptide-MHC complexes. *Nature* 375(6527):148–151.
58. Huppa JB, et al. (2010) TCR-peptide-MHC interactions in situ show accelerated kinetics and increased affinity. *Nature* 463(7283):963–967.
59. Hui E, Vale RD (2014) In vitro membrane reconstitution of the T-cell receptor proximal signaling network. *Nat Struct Mol Biol* 21(2):133–142.
60. Lever M, Maini PK, van der Merwe PA, Dushek O (2014) Phenotypic models of T cell activation. *Nat Rev Immunol* 14(9):619–629.
61. McKeithan TW (1995) Kinetic proofreading in T-cell receptor signal transduction. *Proc Natl Acad Sci USA* 92(11):5042–5046.
62. Kalergis AM, et al. (2001) Efficient T cell activation requires an optimal dwell-time of interaction between the TCR and the pMHC complex. *Nat Immunol* 2(3):229–234.
63. Valitutti S (2012) The serial engagement model 17 years after: From TCR triggering to immunotherapy. *Front Immunol* 3:272.
64. Kusumi A, et al. (2005) Paradigm shift of the plasma membrane concept from the two-dimensional continuum fluid to the partitioned fluid: High-speed single-molecule tracking of membrane molecules. *Annu Rev Biophys Biomol Struct* 34:351–378.

65. Liu B, Chen W, Evavold BD, Zhu C (2014) Accumulation of dynamic catch bonds between TCR and agonist peptide-MHC triggers T cell signaling. *Cell* 157(2):357–368.

66. Melenhorst JJ, et al. (2008) Detection of low avidity CD8(+) T cell populations with coreceptor-enhanced peptide-major histocompatibility complex class I tetramers. *J Immunol Methods* 338(1-2):31–39.

67. Wooldridge L, et al. (2010) CD8 controls T cell cross-reactivity. *J Immunol* 185(8): 4625–4632.

68. Chen J-L, et al. (2000) Identification of NY-ESO-1 peptide analogues capable of improved stimulation of tumor-reactive CTL. *J Immunol* 165(2):948–955.

69. O'callaghan CA, et al. (1999) BirA enzyme: Production and application in the study of membrane receptor-ligand interactions by site-specific biotinylation. *Anal Biochem* 266(1):9–15.

70. Beemiller P, Jacobelli J, Krummel M (2012) Imaging and analysis of OT1 cell activation on lipid bilayers. *Protoc Exch*, 10.1038/protex.2012.028.

71. Ripley BD (1979) Tests of randomness for spatial point patterns. *J R Stat Soc B* 41(3): 368–374.

72. Perry GLW (2004) SpPack: Spatial point pattern analysis in Excel using Visual Basic for Applications (VBA). *Environ Model Softw* 19(6):559–569.